



Computer Methods in Biomechanics and Biomedical Engineering

ISSN: 1025-5842 (Print) 1476-8259 (Online) Journal homepage: <http://www.tandfonline.com/loi/gcmb20>

Detailed finite element modelling of deep needle insertions into a soft tissue phantom using a cohesive approach

Matthew Oldfield, Daniele Dini, Gianpaolo Giordano & Ferdinando Rodriguez y Baena


To cite this article: Matthew Oldfield, Daniele Dini, Gianpaolo Giordano & Ferdinando Rodriguez y Baena (2013) Detailed finite element modelling of deep needle insertions into a soft tissue phantom using a cohesive approach, Computer Methods in Biomechanics and Biomedical Engineering, 16:5, 530-543, DOI: [10.1080/10255842.2011.628448](https://doi.org/10.1080/10255842.2011.628448)

To link to this article: <https://doi.org/10.1080/10255842.2011.628448>



Published online: 10 Jan 2012.



Submit your article to this journal 



Article views: 924



Citing articles: 24 View citing articles 

Detailed finite element modelling of deep needle insertions into a soft tissue phantom using a cohesive approach

Matthew Oldfield*, Daniele Dini¹, Gianpaolo Giordano² and Ferdinando Rodriguez y Baena³

Department of Mechanical Engineering, Imperial College, Exhibition Road, London SW7 2AZ, UK

(Received 2 February 2011; final version received 27 September 2011)

Detailed finite element modelling of needle insertions into soft tissue phantoms encounters difficulties of large deformations, high friction, contact loading and material failure. This paper demonstrates the use of cohesive elements in high-resolution finite element models to overcome some of the issues associated with these factors. Experiments are presented enabling extraction of the strain energy release rate during crack formation. Using data from these experiments, cohesive elements are calibrated and then implemented in models for validation of the needle insertion process. Successful modelling enables direct comparison of finite element and experimental force–displacement plots and energy distributions. Regions of crack creation, relaxation, cutting and full penetration are identified. By closing the loop between experiments and detailed finite element modelling, a methodology is established which will enable design modifications of a soft tissue probe that steers through complex mechanical interactions with the surrounding material.

Keywords: needle insertion; cohesive elements; soft tissue; finite element method; fracture toughness; flexible probe

1. Introduction

A soft tissue probe is being developed at Imperial College London, which is based on a biomimetic design. Inspired by the ability of ovipositing wasps to penetrate both hard substances, indicating a robust design, and target host larvae, indicating a flexible and steerable capability (Vincent and King 1995), a four-part, flexible probe has been designed that emulates these key characteristics (Frasson et al. 2010). Figure 1 shows the flexible probe design and the capability of the four segments to move independently of each other. It is anticipated that, for example, in the future the probe will be used to improve procedures coming under the broad category of minimally invasive surgery. The capability to steer the probe through soft tissue offers the benefits of increased targeting accuracy and movement along more free trajectories. Prototypes of the probe have been shown to be capable of steering along paths of multiple curvatures (Ko et al. 2010). By controlling the offset of the leading probe segment in these actuation schemes, the radius of curvature has been altered in both magnitude and sense allowing the probe to be steered towards a target while avoiding critical obstacles. Ko et al. (2010) have also shown that, within gelatine, a linear relationship exists between the offset of the leading segment and the curvature response of the four-part prototype.

To date, intuitive understanding of the probe–tissue interactions that cause this steering mechanism has been made based on the work of Misra et al. (2010), Wood et al.

(2010) and Ko et al. (2010) on bevel-tipped needles. However, a more thorough understanding of these interactions is required for further development of the probe and implementation in control algorithms. Numerical modelling is an ideal complement to experimental observation for this task, and finite element methods, in particular, offer a rich depth of diagnostic and developmental information. Before finite element models investigating the steering mechanism of the flexible probe can be produced, it is necessary to (i) implement an appropriate failure mechanism for cutting and insertion in the finite element model; (ii) perform experiments that can provide parameters for the material's constitutive behaviour and failure criterion and (iii) validate the finite element models against accepted needle insertion characteristics. These represent the aims of the investigation presented here.

This paper presents a method for detailed modelling of the insertion of a probe into a soft tissue phantom. In overcoming large deformation and friction, substantial progress has been made in the use of cohesive elements in needle insertion simulations including demonstration of the creation of internal surfaces in a tissue phantom and contact loading. The generic force–displacement profile for needle insertions (Shergold and Fleck 2005; Azar and Hayward 2008) is extracted from high-resolution finite element models and validated against experiments to match the significant characteristics of physical behaviour. The level of detail in the finite element model coupled with successful modelling of damage, matching of the force–displacement response and a mechanism for calibrating

*Corresponding author. Email: m.oldfield@imperial.ac.uk



Figure 1. Configuration of the soft tissue probe illustrating its four segments. A lead offset in one segment, used to generate curved trajectories, is also shown.

cohesive elements in the needle configuration are shown for, what is believed to be, the first time.

The characteristics of the force–displacement profiles have proven particularly useful at identifying different regions associated with, for example, puncture and penetration, as well as extracting material and interaction parameters. Needle insertion tests have been performed in the past with a view to extracting the force–displacement response (Howard et al. 1999; Frick et al. 2001) and in (Kataoka et al. 2002) to separate the tip force and the friction force along the needle shaft. Other tests have been used, in part, to establish the fracture toughness of the penetrated material (Shergold and Fleck 2005; Azar and Hayward 2008). The materials covered in these investigations are either specific tissues or isotropic substitutes that are stiffer and tougher than the gelatine soft tissue phantom used in this investigation. An attempt is made to use the extracted parameters in finite element solutions by Misra et al. (2008), but no effort is made to use the model and experiment to corroborate each other. Shergold and Fleck (2004) use finite elements to aid in the extraction of the fracture toughness, but do not implement their experimental findings: establishing the fracture toughness and the nature of the insertion mechanics being indeed a comprehensive task in itself. The work by Simone and Okamura (2002) recreates needle insertions into liver with some success by implementing a cutting force. Here, the use of a geometry-independent material parameter to define failure, rather than a needle-specific cutting force, is contemplated.

It should be noted, however, that cutting force measurements are particularly well suited to simplified finite element models of the type used in rapid feedback simulations. A variable needle insertion force along its shaft is implemented by DiMaio and Salcudean (2002). This model is used, for simulation purposes, in rapid feedback models of limited resolution and also applied in the identification of the substrate material properties (DiMaio and Salcudean 2003). A similar reduced resolution finite element model with stick/slip friction forces along the shaft was used for path planning using a bevel tip by Alterovitz et al. (2005) and developed into a 3D environment with a 1D needle by Chentanez et al. (2009).

Finite element analysis is established as one of the most popular tools for needle insertion modelling.

However, numerical descriptions of needle insertions require a means of describing the failure of the tissue as the probe advances. This presents a considerable technical challenge that has been approached in a number of ways depending on the final application. In surgery simulators, cutting forces and mesh adaptation are often accomplished with simplification of geometries and amalgamation of many interaction forces (Courtecuisse et al. 2010; Zerbato et al. 2010). Despite the advantages of the rapid feedback rates provided, this type of approach lacks the detail to be able to inform design improvements. Virtual internal bond methods offer more local modelling of crack formation (Gao and Klein 1998; Zhang and Ge 2005). However, virtual internal bond algorithms are not widely adopted in commercial finite element software. Recent advances to include element partition as part of the extended finite element method (Pannachet et al. 2009) and the finite cover method (Terada et al. 2007) are extremely powerful at predicting crack paths. However, the applicability of the residual crack surfaces for contact loading has not been demonstrated.

Cohesive elements have been widely utilised in crack propagation analysis (Chen et al. 1999; Song et al. 2006; Geißler et al. 2010) as they allow the inclusion of active surfaces as the simulation develops and are also implemented in commercial finite element software. An initial attempt to use these techniques in modelling needle insertions is provided by Misra et al. (2008). Cohesive elements allow flexibility as they only need to be deployed along the insertion path (which in turn can be computed ‘on the fly’). Therefore, simple adaptive remeshing algorithms can be successfully employed to refine the finite element models where needed. This enables very detailed investigations at small scales. Experiments are required to define the fracture toughness, but the cohesive element’s simple formulation and ease of incorporation into existing models with normal, shear and combined load conditions make them ideally suited to the work undertaken here.

To effectively model the processes occurring during steering of the biologically inspired flexible probe, detailed analysis of the interactions with a substrate (e.g. a tissue phantom) is required. In Section 2, an energy approach to crack propagation is outlined and Section 3 illustrates how cohesive elements within finite element models use this energy to implement model failure. The experimental method and corresponding finite element tests performed on a gelatine phantom are described in Sections 4 and 6. Results from these tests and discussion of them are presented in Sections 5 and 7–9. Finally, conclusions and proposals for future work are included in Section 10.

2. Establishing the strain energy release rate for a crack

When modelling the passage of a needle or probe through a tissue phantom, an appropriate methodology for representing the failure of the material is required. In a linear elastic model, the strain energy release rate, G_c , is an effective description and is used by Sanford (2003) to detail the mechanical concept of crack creation. This approach is adopted here, as it can be implemented in finite element models through cohesive elements.

In the work of Azar and Hayward (2008), Shergold and Fleck (2005) and Misra et al. (2008), G_c is extracted from deep needle insertion tests. Two principal advantages of this type of test are as follows: the experimental method is highly analogous to the type of mechanics of the flexible probe in operation and G_c can be obtained with reasonable accuracy from a phantom which is too flexible and weak to maintain its integrity in other experimental procedures.

During a through-and-through penetration of a soft tissue phantom, several phases exist, shown in Figure 2:

- Initial deformation prior to puncture; external work is converted to strain energy (region A).
- Initial crack propagation and relaxation of the tissue phantom (region B).
- Crack propagation until full penetration; the external work is balanced by the energy required to create a crack, the strain energy required to open the crack and deform the surrounding material and the work required to overcome friction (region C).
- Sliding after full penetration; after another period of relaxation (region D), the external work is only counteracting the frictional sliding between the probe and the crack that extends through the depth of the phantom (region E).

Using force–displacement plots, experimental measurements of crack size and finite element simulations to predict strain energy, G_c , can be extracted by the elimination process described by Azar and Hayward

(2008), Shergold and Fleck (2005), Misra et al. (2008) and Simone and Okamura (2002). This is summarised by the following generic energy balance:

$$W_{\text{ext}} = W_f + W_\varepsilon + W_{G_c}, \quad (1)$$

where W_{ext} is the external work supplied by the needle, W_f is the work to overcome friction, W_ε is the work converted to strain energy in deforming the material and W_{G_c} is the work required to create the crack. This energy balance is applied, with assumptions appropriate to deep needle insertions, to extract the strain energy release rate in Equations (2)–(6). The frictional force F_f is assumed to vary linearly from zero at no insertion to a maximum value F_{max} when the needle has fully penetrated the phantom (Azar and Hayward 2008; Misra et al. 2008):

$$F_f = \begin{cases} \frac{(F_{\text{max}}x)}{d}, & \text{if } 0 < x \leq d, \\ F_{\text{max}}, & \text{if } x > d, \end{cases} \quad (2)$$

$$W_f = \int_0^{u_p} F_f(x) dx, \quad (3)$$

where x is the displacement along the crack axis and d is the depth of the gelatine tissue phantom. For $0 < x < d$, u_p is the insertion depth of the needle tip and, except for small insertion depths prior to crack propagation, the tip displacement and crack length are assumed to be equal.

The amount of work that is used to deform the tissue phantom during the insertion process is given by Equation (4) based on the approach by Shergold and Fleck (2004, 2005). This deformation may be elastic, hyperelastic, permanent or recoverable. Throughout this paper, possible rate-dependent effects are ignored to simplify the process, leaving

$$W_\varepsilon = \int_0^{u_p} U_\varepsilon dx, \quad (4)$$

where U_ε is the strain energy per unit length generated due to crack propagation and penetration. The reaction force F_R and needle insertion depth give

$$W_{\text{ext}} = \int_0^{u_p} F_R dx. \quad (5)$$

By a process of elimination, the energy required to create the crack surfaces along which the probe traverses (W_{G_c}) can be established if the crack width $w(x)$ is known (Shergold and Fleck 2005; Azar and Hayward 2008). Consequently, the strain energy release rate, G_c , is

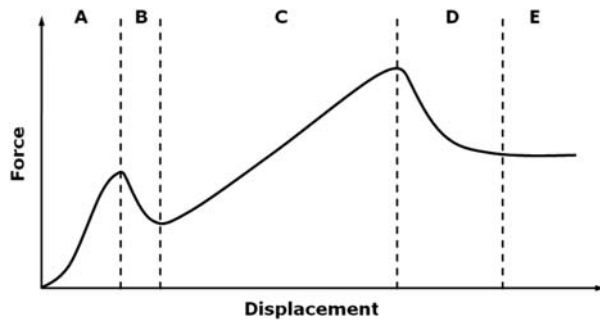


Figure 2. The five generic stages of through-and-through needle insertion into a soft solid.

obtained as follows:

$$W_{G_c} = \int_0^{u_p} G_c w(x) dx. \quad (6)$$

3. Energy approaches to crack propagation in finite element models

Within the context of finite element modelling, the ‘energy of fracture’ approach is a very effective method of incorporating failure of an otherwise continuous mesh. In ABAQUS finite element software, cohesive elements implement this concept through a fracture toughness parameter which is analogous to the strain energy release rate by Sanford (2003).

In 2D simulations, the cohesive elements are four-noded with two ‘active’ faces. The traction–separation relationship between these two faces of the element determines whether or not the cohesive element is intact or, having failed, is removed from the simulation. A particular advantage of this type of element is that it can be specified with zero geometrical thickness and can thereby seamlessly be included within an apparently continuous mesh. To incorporate elements of zero thickness, a constitutive thickness parameter (T_c) is included in the element formulation linking strain (ε) and separation (δ):

$$\varepsilon_{n,s} = \frac{\delta_{n,s}}{T_c}, \quad (7)$$

where n and s refer to the normal and shear separations between the active faces of the elements.

T_c is set to unity thereby equating the displacement and strain. The traction vector $\{\mathbf{t}\}$ can then be linked to the strains $\{\varepsilon\}$ via the stiffness matrix $[\mathbf{K}]$:

$$\begin{Bmatrix} t_n \\ t_s \end{Bmatrix} = \begin{bmatrix} K_{nn} & K_{ns} \\ K_{ns} & K_{ss} \end{bmatrix} \begin{Bmatrix} \varepsilon_n \\ \varepsilon_s \end{Bmatrix}, \quad (8)$$

which in turn links the separations, constitutive thickness and tractions in the normal and shear directions. Further details of the formulation of the cohesive elements are available in ABAQUS (2009).

The area underneath the curve (G_c) linking traction and separation in Figure 3 is the strain energy release rate parameter. A bilinear profile has been implemented for the traction–separation relationship as it is readily available within ABAQUS software and sufficient for the modelling performed here. Alternative trapezoidal and exponential traction–separation models are examined more closely by Alfano et al. (2009).

By inserting these four-noded elements into the connectivity of a 2D, plane strain mesh, it is possible to model the failure of the continuous material across the cohesive element. When failure has occurred as a result of

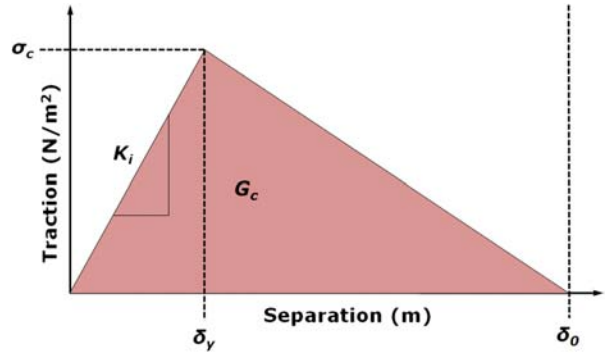


Figure 3. Traction–separation relationship for cohesive elements, which is used to implement damage in the finite element mesh.

the separation exceeding δ_0 , the cohesive element is removed from the simulation to leave behind an extended crack surface. For the needle insertion experiments described here, it is assumed that the crack path can be predetermined. The symmetry of the needle and tip, the symmetry of the insertion point relative to the boundary conditions applied to the gelatine and the homogeneity of the gelatine itself dictate that the crack path would follow the needle insertion axis. It is therefore sufficient to add a single layer of cohesive elements to the mesh (Oldfield et al. 2010).

Where it is not possible to predetermine the crack path, a popular approach is to distribute cohesive elements between continuum elements over an area where the crack can be expected to propagate. This approach has proved successful for predicting a previously unknown crack path (Song et al. 2006). It is, however, preferable to avoid this approach when it is unnecessary for two principal reasons. Firstly, the computational cost of including cohesive behaviour, and the resulting substantial increase in the number of degrees of freedom, can be significant. Secondly, the global behaviour can be detrimentally altered by a process known as ‘artificial compliance’, which is well described by Geißler et al. (2010).

4. Experimental extraction of strain energy release rate for gelatine

A consistent soft-tissue phantom is required for experimental development of the probe described in Section 1. Gelatine has proved an excellent substitute for real tissue as it enables material parameters to be controlled depending on the percentage weight of powder used. Variations between tests, and complexities associated with anisotropy and inhomogeneity of biological tissue, are eliminated due to the isotropic nature of the resulting phantom.

Previous in-house experiments have established that a 6% by weight of gelatine powder (Dr Öetker beef gelatine)



Figure 4. The three, rigid, needle tip designs attached to an 8-mm needle: from left to right, conical, prismatic and double-edged, with a 50° included angle.

has a similar Young's modulus (E) in tension to porcine brain. This value of 7 kPa fits within the range of values by Franceschini (2006), but is at the low extremity of the surveyed data.

An 8-mm diameter silver steel needle was used for the insertion tests. To establish a value for the strain energy release rate that was independent of geometrical parameters, three different shaped tips, each with an included angle of 50°, made from a relatively rigid rapid prototyping material Vero White (Objet Geometries Ltd., Rehovot, Israel), were used for the penetration tests. The tips were conical, prismatic and double-edged in shape as shown in Figure 4.

All experiments were conducted in gelatine 86 mm deep and at $20 \pm 3^\circ\text{C}$ which was measured internally by an analogue thermometer. An Instron Machine (model

number: 5565) with a 100 N drop through load cell (2525-807 series) inserted the needle from outside the gelatine until a displacement of 230 mm at a constant speed of 1 mm/s (Figure 5). This ensured that viscoelastic effects were reduced and that through-and-through penetration was achieved. Once full penetration had been attained, enough time remained for any gelatine relaxation to occur (region E in Figure 2) to enable accurate extraction of the maximum friction force F_{\max} in Equation (2). Three insertion tests per tip shape were performed at different locations in the gelatine container to obtain an average and limit the effect of temperature variations and any fluctuations in material properties across the block. Force measurements were made at increments of 0.1 mm insertion.

The crack width, $w(x)$, is important for two reasons: to build finite element models capable of extracting U_e and to establish the crack area, for a given insertion depth, when calculating G_c . Although slices through the gelatine revealed that the crack width was not constant, an average was sought to simplify these calculations. Where the gelatine's integrity permitted, and where a crack could be identified in its closed state, measurements of the crack width were taken on the top surface and from slices at depths of 30 and 50 mm following needle extraction. For the full insertion depth of 86 mm, a second-order polynomial was fitted to the three measured crack widths at different depths. The quadratic curve was then used to generate a mean crack width \bar{w} for the full gelatine depth.

To calculate W_e , the strain energy per unit length of insertion (U_e) is required. It is assumed that the majority of this strain energy comes from deforming the newly created

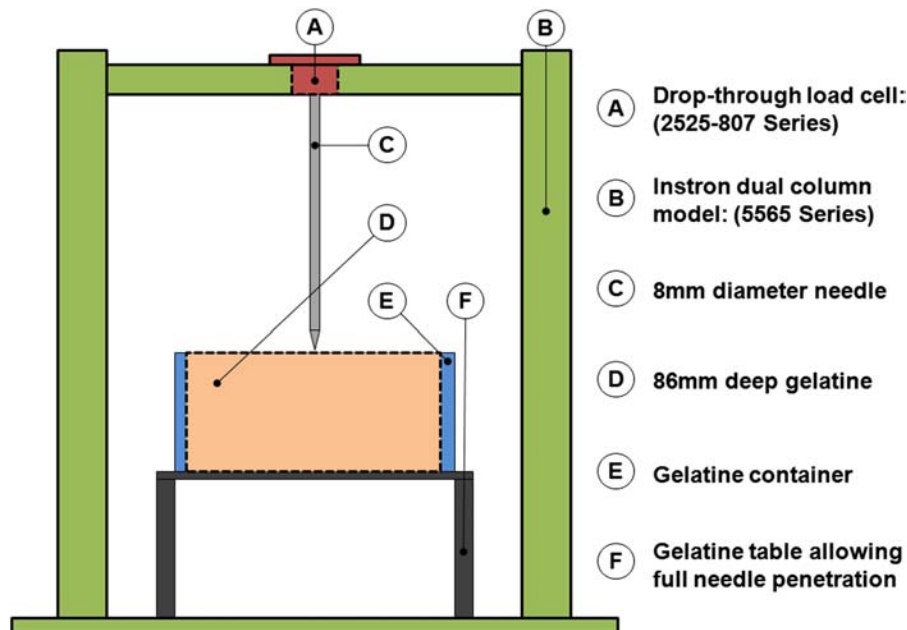


Figure 5. The principal experimental components used for the through-and-through needle insertion tests.

crack surface in the gelatine to the profile of the needle. A finite element simulation was created to establish the parameter U_ε using the approach of Shergold and Fleck (2004). In this method, a plane strain model in the x - y plane is used to deform a pre-existing crack surface in gelatine to the profile of the 8-mm needle. The average width of the crack surface (\bar{w}) is established using the experimental method described previously in this section.

By including the crack in a relatively large block of 640 mm \times 640 mm, the impact of external boundary conditions on the strain energy is minimised. Boundary conditions enforcing symmetry in the x and y axes are applied to the internal edges of the model, with only the nodes on the crack surface, of length $\bar{w}/2$ due to symmetry, free to move. The gelatine is assumed to be linearly elastic. A 4-mm radius rigid surface was adopted to deform the gelatine until it had reached the configuration associated with the point at which the needle diameter had forced the crack fully apart. Linear elements, which were highly concentrated around the crack zone, and an implicit solver in ABAQUS were used to extract U_ε in the gelatine. The finite element model is shown in its final configuration in Figure 7. The value of U_ε was inserted into Equation (4) to give a value of W_ε for an insertion depth of 86 mm. The value of W_ε was assumed to be constant for all experiments with an 8-mm diameter needle.

5. Results of the needle insertion tests

Measurements of the crack width at various depths in the gelatine resulted in a mean value of $\bar{w} = 15$ mm for an 8-mm diameter needle. This value can only be considered

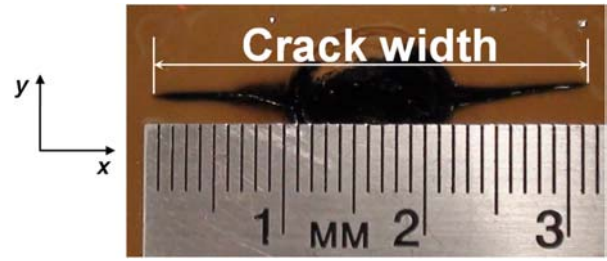


Figure 6. Essentially planar crack in gelatine caused by needle insertion, which is formed by an 8 mm needle with a 50° prismatic needle tip and viewed on the top surface of the gelatine (looking along the z -axis in Figure 5).

partially accurate due to the difficulties in establishing the crack profile through the depth of the gelatine. One particular difficulty was that the crack closed up after needle extraction and identifying its limits was difficult. The crack can be considered planar, as Figure 6 shows, even though some more local damage may be occurring around the needle tip.

Deforming a 15-mm crack with an 8-mm needle as described in Section 4 gives the response shown, for quarter symmetry, in Figure 7. This plot of only a small part of the gelatine volume demonstrates that most of the strain energy is highly localised to the crack. The stress is concentrated around the edge of the crack, and substantial compression and contact pressure occur at the crack's midpoint. Using $E = 7$ kPa, established by tensile tests on the gelatine, and a Poisson's ratio $\nu = 0.475$, to approximate incompressible behaviour, the recoverable strain energy was found to be 73.20×10^{-3} J/m

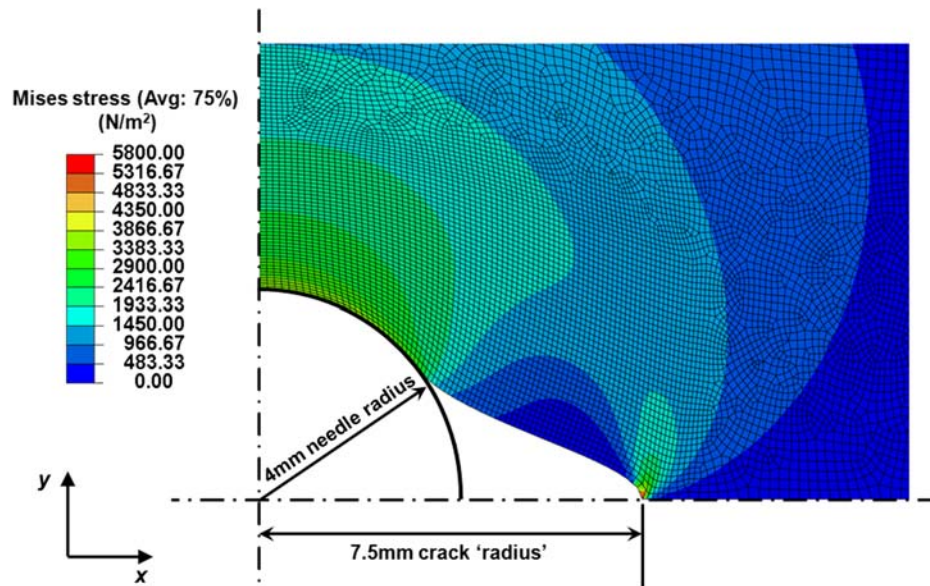


Figure 7. Mises stress distribution in a quarter symmetry simulation. Used to establish U_ε for an 8-mm diameter needle and 15-mm crack in an 640 mm \times 640 mm block with $E = 7$ kPa and $\nu = 0.475$.

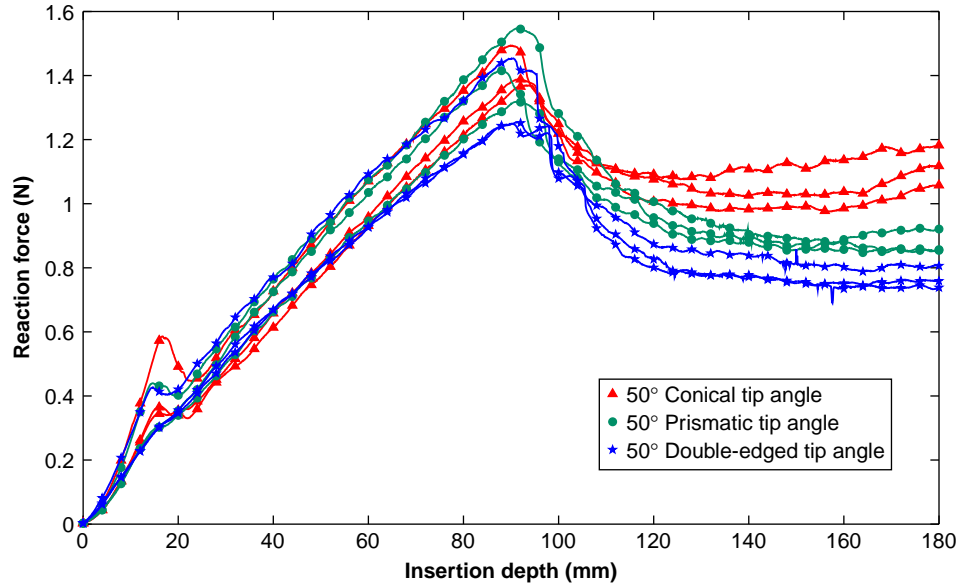


Figure 8. The force–displacement response for nine experimental needle insertions, with three different tip designs, through a gelatine depth of 86 mm.

and, therefore, for a gelatine block 86 mm deep $W_g = 6.30 \times 10^{-3}$ J.

Figure 8 shows the force–displacement profiles for the nine needle insertion tests described in Section 4. There is consistency between the nine tests, with all of them showing five stages, defined in Section 2, for penetration. Although the experimental results for the needle insertions show grouping, regardless of geometry, until the end of the cutting phase (Figure 8), the subsequent steady-state phase is clearly separated according to the tip shape. These variations in response are assumed to be attributed to inconsistencies in the gelatine between tests. The variability of the initial response, and the scatter between the tests characterised by the same tip geometry, can be at least in part attributed to the fact that the gelatine stiffness is very sensitive to temperature changes and only limited temperature control was applied during the experiments.

Average values for the essential output parameters from Figure 8 are given below and in Table 1. These are computed from individual output parameters rather than from a mean force–displacement profile – guaranteeing the character of each force–displacement profile. As such, the cutting process is assumed to occur from a point 86 mm – the gelatine depth – before the maximum insertion force to the point of maximum force. Using

this approach, the mean experimental parameters for the nine needle insertions are $F_{\max} = 0.919$ N, $W_f = 39.99 \times 10^{-3}$ J and $W_{G_c} = 22.48 \times 10^{-3}$ J. This leads to a mean strain energy release rate of $G_c = 17.43$ J/m².

6. Finite element simulation methodology

To model the full crack propagation process in 3D would prove prohibitively costly. Instead, an approximate plane strain simulation was constructed. A rigid body and reference node replaced the relatively rigid needle used during experimental testing. The reference node provided the point at which displacement boundary conditions were applied as an input and reaction forces on the needle were obtained. The needle had a width of 8 mm and an included angle at the tip of 50° to correspond with the dimensions of the needle and tips used in the experimental test.

The gelatine block was modelled using three-noded, plane strain, elements with a Young's modulus of 7 kPa to match the material used experimentally. A Poisson's ratio, ν , of 0.475 was used to approximate almost incompressible conditions in the gelatine. The block was 86-mm deep to match the experimental insertion depth and 160-mm wide to ensure that effects of the vertical boundaries

Table 1. Comparison of the work and energy parameters for experimental tests and finite element simulations.

	External work (J)	Cutting work (J)	Friction work (J)	Strain energy (J)
Experimental mean	0.069	0.022	0.040	0.006
Finite element with no cohesion	0.058	N/A	0.052	0.006
Finite element with cohesion	0.084	0.022	0.059	0.004

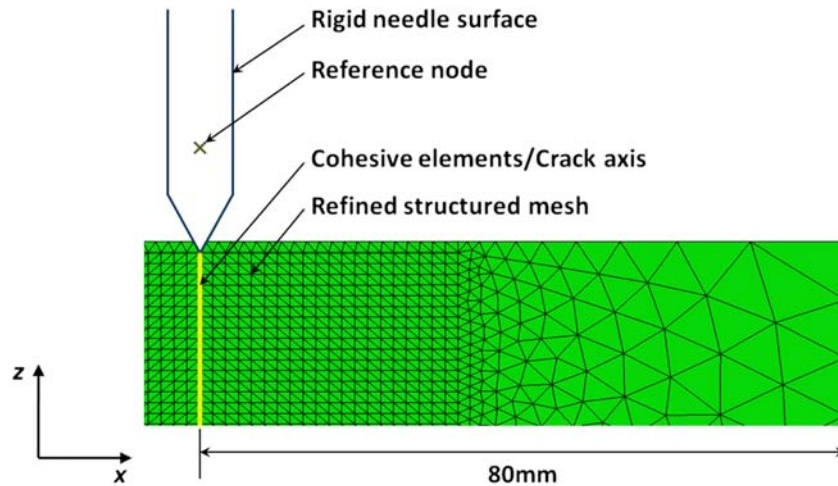


Figure 9. Key features of the finite element model with cohesive elements along the crack axis in the 86-mm deep gelatine block.

on the insertion were minimised. An out-of-plane depth of 15 mm was determined by the mean planar crack dimension, \bar{w} , established in Section 5. Element resolution was concentrated around the insertion axis with a structured mesh used in this region that extended 32 mm on either side. The element width and height used in this highly resolved zone was 1.6 mm, which can be seen in Figure 9. The element size and mesh configuration, when tested, also demonstrated convergence in comparison with considerably more refined meshes.

All contact in the model was defined using the penalty contact algorithm (ABAQUS 2009). Frictionless contact interfaces were defined between the faces of the gelatine on either side of the predetermined crack path. This prevented interpenetration of the unconnected faces throughout the simulation. Contact between the needle tip and the crack surfaces was also assumed to be frictionless. The long edges of the needle had frictional contact with the gelatine, with friction defined using a Coulomb friction law.

Boundary conditions were applied that approximated the experimental environment as closely as possible. The sides of the gelatine block were 'pinned' to replicate the influence of the gelatine container. Nodes along the bottom of the gelatine block were free to move laterally, but prevented from normal motion. An additional constraint of equal and opposite displacements was applied to the nodes on either side of the crack axis to reduce the likelihood of buckling associated with small numerical errors. To enable initial separation across the crack surface, two elements at the top of the gelatine block were removed so initial contact caused a lateral force across the cohesive elements. The simulation was performed using ABAQUS software (version 6.9) and an explicit solver.

Two sets of experiments were performed, with the first using needle insertions without cohesive elements to

isolate the frictional response of the interaction with gelatine. The coefficient of friction, μ , was given a minimum value of zero and a maximum value of 0.5 with increments of 0.1. Through-and-through penetrations were achieved by a 160-mm displacement at a rate of 10 mm/s. This improved the time to complete the simulation while ensuring quasi-static conditions, monitored using the kinetic energy output.

In the second set of experiments, cohesion was included through four-noded, plane strain, cohesive elements along the axis of insertion. These elements had no geometric thickness, a constitutive thickness (T_c) of unity and length of 1.6 mm. $G_c = 17.43 \text{ J/m}^2$ (Section 5) was implemented to match the experimental strain energy release rate and the value of μ was used from the first set of numerical tests that represented the best match with experimental results. δ_y and δ_0 were varied to obtain the closest match for the pre-puncture force–displacement profile.

7. Results of the finite element simulations

The undamped dynamic response from the explicit solver results in considerable high-frequency vibrations in the measured reaction force. Consequently, this output is post-processed using a moving average procedure designed for the highest observable frequency.

Figure 10 shows that during insertion without cohesive elements, there is still some relaxation of the gelatine that is dependent on the value of μ . For $\mu = 0.4$ and 0.5, this relaxation is insignificant, while for lower values of μ , it is much more apparent. Following this relaxation, the reaction force increases in an essentially linear relationship with insertion depth. After the tip's emergence through the base of the gelatine block, the reaction force decreases slowly and tends to a steady-state value (F_{\max})

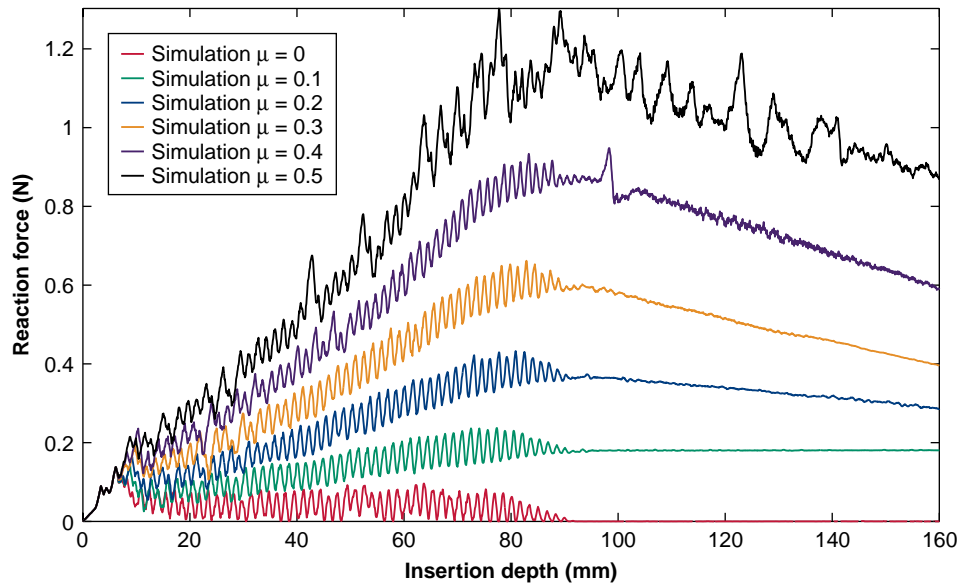


Figure 10. Impact on the reaction force of different friction coefficients, μ , demonstrating how increased insertion distance causes behaviour analogous to a spring.

that is dependent on μ . In the frictionless state, this steady-state value is, as anticipated, zero, with F_{\max} increasing with the value of μ .

This linear increase in friction force during insertion is also revealed in Figure 14, where the frictional energy dissipation is shown. For the frictionless case, this is always zero, but for the remaining simulations, once the probe shaft comes into contact with the side of the gelatine, the energy dissipated due to friction rises in a manner that is essentially quadratic. This is true for all values of μ and verifies the approach used by Misra et al. (2008) and in Equation (2).

From these models without cohesive elements, comparison between Figures 8 and 10 shows that the increasing force during cutting is due to the friction between the needle shaft and crack surfaces. For $E = 7 \text{ kPa}$, $\mu = 0.5$ gives the closest agreement to the rate of increase of this force.

When incorporating cohesive elements with established values of G_c , the tuning parameters in the relationship shown in Figure 3 are δ_0 and δ_y . Figure 11 illustrates the effect that these parameters have on models where all other parameters are maintained, i.e.

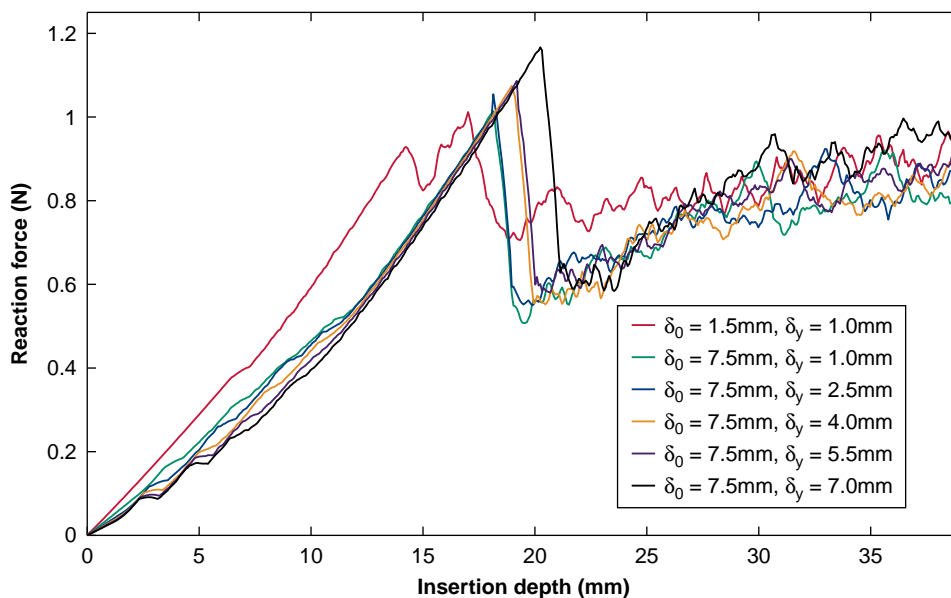


Figure 11. Influence of δ_y and δ_0 on the force–displacement response, notably the initial stiffness, at the early stage of insertion.

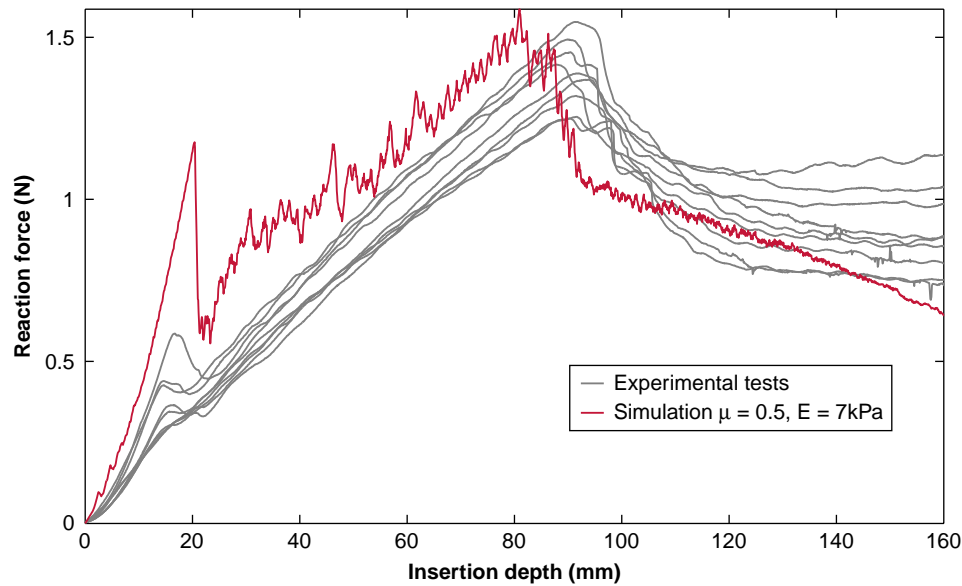


Figure 12. Comparison of the experimental and simulated force–displacements for complete penetration of a gelatine block. Addition of cohesive elements dramatically improves the response characteristics (see also Figure 10).

$G_c = 17.43 \text{ J/m}^2$, $E = 7 \text{ kPa}$ and $\mu = 0.5$. Although the impact post-relaxation is limited, the force–displacement response in region A of Figure 2 can be tuned to some degree, and the initial stiffness is best matched when $\delta_y = 7$ and $\delta_0 = 7.5 \text{ mm}$.

8. Comparison of finite element and experimental results

There are two areas for comparison between the experimental and modelled needle insertions: the energy response, shown in Table 1, and the force–displacement profile of Figure 12.

Table 1 shows that the amount of external work provided in the finite element simulations is greater than in the experimental tests. As the cohesive element parameters and out-of-plane depth of the finite element model are directly calibrated from the experimental tests, it is inevitable that the work to cause crack propagation matches exactly. Good agreement is also achieved between the strain energies. However, the contribution of recoverable strain energy is small and discrepancies are not directly significant to the overall agreement between the model and the experiment. In the finite element models, with and without cohesion, the amount of energy dissipated due to frictional sliding is similar. It is this frictional response that is the principal cause of the extra work that the needle has to perform during the modelled insertion.

This additional work is apparent from Figure 12 in the increased area under the force–displacement plot for the finite element model. A peak force, considerably greater than that seen experimentally, is required to cause failure

of the first cohesive element and initiate crack propagation. Following relaxation, the modelled force becomes much closer to the experimental response, and although the modelled force is consistently greater during the crack propagation phase, the rate at which it increases matches the experiments well. Due to the slightly earlier onset of final failure, the peak experimental and modelled forces are also in good agreement.

However, agreement is not so good in the steady-state frictional force F_{\max} and in the sharpness of the relaxations (regions B and D in Figure 2). F_{\max} is not constant, but continually declines following failure of the final cohesive element, yet the range of force is comparable with the experimental response to an insertion nearly twice the gelatine depth. Despite these discrepancies, all of the phases of Figure 2 are captured by the finite element model, with comparable forces, in a way that is not possible without cohesion (Figure 10).

9. Discussion

There are some small but perceivable variations in the experimental response attributed to internal temperature variation of the gelatine phantom during experiments (Section 5 and Figure 8). Despite this, the overall experimental response displayed many consistent characteristics that could be used to inform and evaluate the finite element models. The steady-state friction force that occurs after full penetration is similar in magnitude to the peak deformation force; a strong indication of the significant contribution of friction to the insertion process. In the controllable soft tissue phantom, the large friction forces

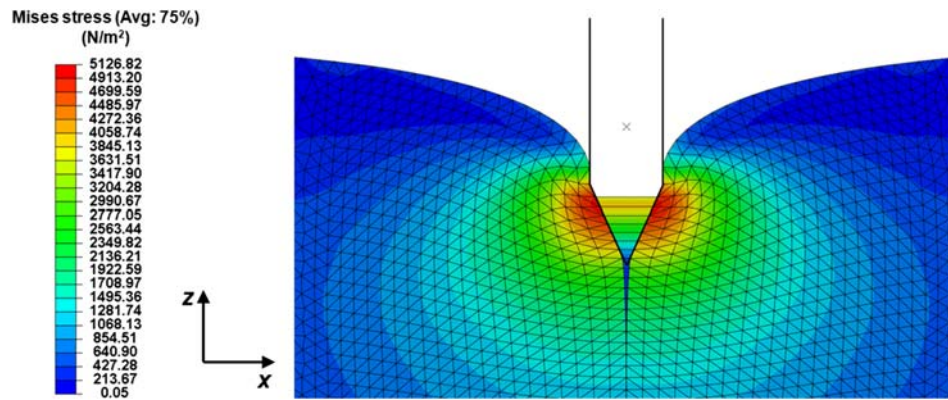


Figure 13. Contours of Mises stress and distortion of the finite element gelatine block immediately prior to failure of the first cohesive element. Interpenetration of the cohesive elements by the needle surface is also shown.

combined with low stiffness of the gelatine make the finite element mesh susceptible to excessive distortion. Particularly during initial crack formation (Figure 13), where the material deforms greatly before relaxation, the finite element model may need adaptive meshing techniques if frictional forces at the tip are included as a model development. The large strains at this point will be better represented by a hyperelastic model in future. Both hyperelasticity and viscoelasticity will also be incorporated into the material definition following further rate-dependent experiments on gelatine.

A demonstration of the advantages of finite element models, even with a simplified material model, is provided by the ability to use the extra information provided from numerical models to understand the needle insertion process. The dense mesh along the needle tip facilitates diagnostic information that cannot be established experimentally. The contact pressures, surface tractions and material stresses are essential output parameters that will guide further design and development of the probe described in Section 1. Features like stress concentrations in the tissue phantom can be seen, and designed out, with the aid of high-resolution models. Similarly, geometries that accentuate lateral forces can be explored without the need for costly prototypes. Cohesive elements have shown themselves to be adept at representing mesh failure at this scale and, as such, are vital to the design and modelling process.

Calibration of the finite element models is made through an iterative process using experimental results. For what is believed to be the first time, the authors have closed the loop between a detailed finite element simulation and the response of a needle insertion into a soft tissue phantom. The result is a model that matches the overall strain energy and strain energy release rate well, and the frictional energy dissipation moderately well. In terms of replicating the force–displacement behaviour of needle insertion experiments, the results are even more encouraging.

Figure 2 illustrates five key aspects of needle insertion experiments. Comparison with Figures 10 and 12 shows the importance of cohesive elements in enabling each of these aspects to be modelled. Significantly, this is achieved with a material constant that is independent of the needle or probe geometry. The overall characteristic shape of the generic needle insertion curve is well represented. It is also anticipated that the addition of rate-dependent materials will not only improve the behaviour of the model in the initial indentation phase prior to puncture, but also result in a more gradual relaxation following initial crack formation and full penetration. A plot of the energies during the simulation (Figure 14) provides additional diagnostic information. This indicates the assumptions made in Section 2 about the processes taking place are accurate. A comparison of the energy dissipated due to friction and the energy due to cutting reveals that, at small insertions, the cutting behaviour is significant, but at deeper insertions the frictional response dominates the cutting response.

Despite good correlation between the numerical model and the experimental behaviour, discrepancies can be attributed to the cohesive elements. Each cohesive element can be considered to have a pair of active faces defined by nodes 1–2 and 3–4. Between these active faces the traction–separation response of Figure 3 is defined. The passive edges defined by nodes 2–3 and 1–4 are, however, free to be penetrated resulting in the needle tip advancing into the cohesive part of the mesh before failure and subsequent cohesive element removal (Figure 13). This is a physically intangible situation, but inevitable due to the combination of cohesive elements and the type of contact loading required to damage them.

In the case of cohesive elements, their capability to represent the energy of crack formation comes at the cost of being unable to prevent this penetration. The impact of the penetration of the probe into the cohesive elements can be mitigated by minimising the parameters δ_y and δ_0 to

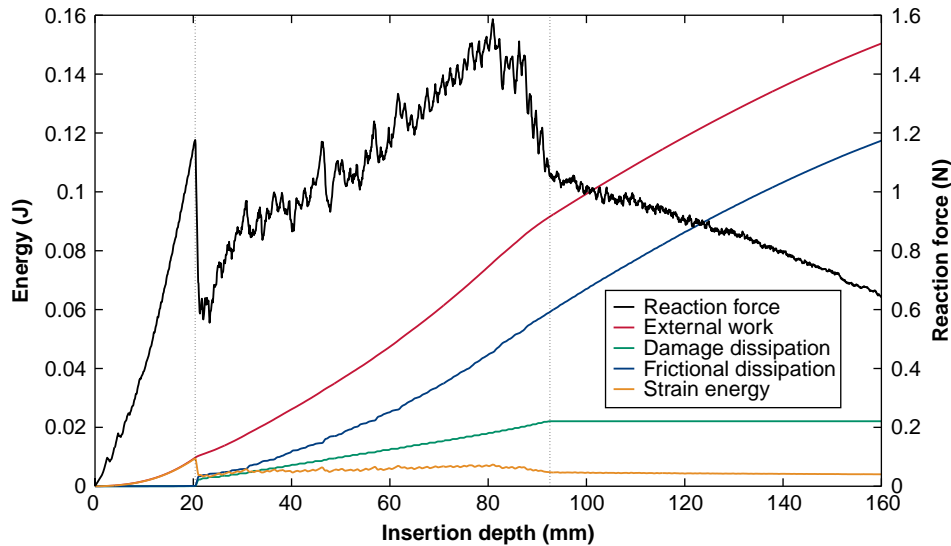


Figure 14. The force–displacement plot with the energy response, demonstrating the capability of finite element models to provide additional insight into the processes taking place. Dashed lines correspond to the onset of damage and the failure of the last cohesive element.

trigger the earliest possible failure and creation of the crack surface. Taking these steps comes at the cost of increasing the stiffness parameter K_i (Figure 3), which in turn tends the simulation towards numerical instabilities. As Figure 11 shows, these measures may also result in a less realistic, and more stiff, force–displacement profile prior to crack creation which, again, can probably be mitigated by the implementation of viscoelastic constitutive laws to describe the gelatine.

Calibration of the cohesive elements is also highly sensitive to measurements of the crack width ($w(x)$). Equation (6) shows that errors in crack width measurement are directly transferred to the estimation of G_c . These errors also impact the somewhat less critical parameters U_ε and hence W_ε via the size of the crack used in the finite element model described in Section 4 and shown in Figure 7. With the exception of the upper surface, measuring the crack width through the gelatine depth was extremely difficult, as the crack closed on needle extraction. This means that values of G_c established for the gelatine soft-tissue phantom are subject to some uncertainty. Where results are available, the crack width at the surface was larger than the crack width developed through the depth. Consequently, the maximum and minimum bounds of the crack width are known from the value measured at the surface and the needle diameter, respectively, and it is felt that the method used to estimate \bar{w} is adequate notwithstanding its limitations. To improve this, the development of more accurate experimental techniques is required to consistently reveal the crack widths following needle insertion.

The presence of cohesive elements is required though to model effectively the deformation of the gelatine close

to the probe tip. Figure 15 shows clearly that omitting the cohesive elements, and beginning the simulation with pre-existing damage result in significantly different behaviour. The stresses around the needle tip are much larger when cohesive elements are present and the gelatine material remains in contact with much more of the needle tip. Even though the energetic processes during the insertion process and the force–displacement relationship itself have been matched, the ultimate tuning of the detailed model can only come through tracking of material displacements and strain in an area highly local to the needle tip. Such an approach is not easily achievable at the level of detail in these finite element simulations with conventional techniques using fiducials. Consequently, it is assumed that the approach using cohesive elements is more realistic due to the previously reported concentration of forces around the needle tip (DiMaio and Salcudean 2002) and the better approximation of continuous, undamaged material at the start of the process.

10. Conclusions and future work

High-resolution finite element tests have been used to validate experimental needle insertions for what is believed to be the first time. Cohesive elements can be used to model the cutting process during needle insertion in high-resolution finite element simulations. As a result of contact loading by the needle, soft tissue phantom and large amount of friction, the deformations and distortions in the finite element model are large. In overcoming these difficulties, the experimentally observed characteristics of puncture, penetration, tissue traversal and re-emergence of the needle are all captured by the finite element model.

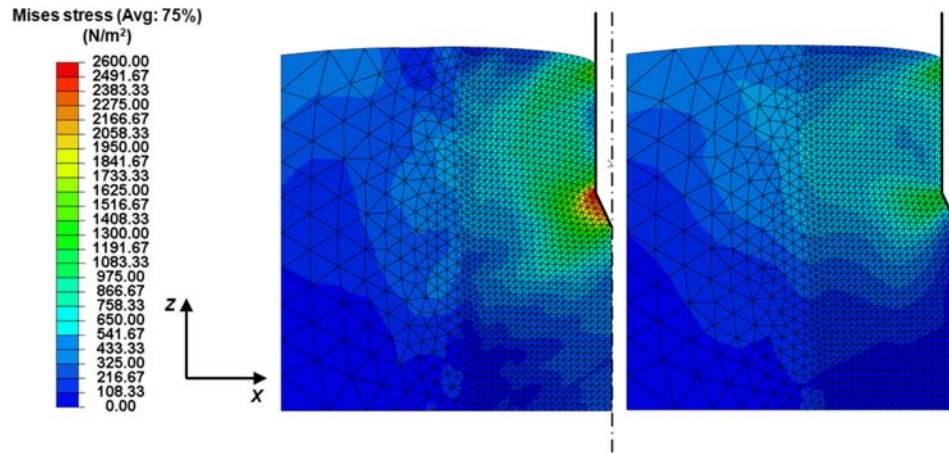


Figure 15. Deformation and Mises stress distribution with cohesive elements (left), not shown, and without cohesive elements (right) after 40 mm of insertion.

Calibration of the cohesive elements can be achieved using diagnostic information available from finite element models, particularly the evolution of different energy parameters during the numerical experiment. For the first time, it has been demonstrated how to close the loop between experimental observations of needle insertions and finite element models of high enough resolution to facilitate design modifications to the tip profile.

The Young's modulus and strain energy release rate are associated with softer biological material than other reported values. The parameters extracted from gelatine, though based on a linear elastic assumption, could be useful for others investigating insertion of needle into, e.g. organic soft tissue. Significantly, making use of the strain energy release rate means that material failure is modelled without reference to geometry-specific cutting forces associated with a given needle or probe design.

Despite the progress reported here, further developments to the modelling process remain. Notably, the gelatine tissue phantom will be more realistically characterised with hyperelastic and viscoelastic behaviours. It has also been seen that, for a complete validation, a technique that will enable high-resolution experimental displacements local to the needle tip needs to be developed. Finally, the cohesive elements will be applied along non-determinant crack paths, which will lead to full models of the steering process of the probe described in Section 1.

Acknowledgements

The research leading to these results has received funding from the European Research Council under the European Union's Seventh Framework Programme (FP7/2007-2013)/ERC grant agreement no. 258642-STING. The authors are also grateful for the support of EPSRC grant EP/E040918/1 and the EU-FP7 Project ROBOCAST (FP7-ICT-21590).

Notes

1. Email: d.dini@imperial.ac.uk
2. Email: gianpaolo.giordano10@imperial.ac.uk
3. Email: f.rodriguez@imperial.ac.uk

References

- ABAQUS. 2009. Abaqus version 6.9 documentation. Providence, RI: Dassault Systemes Simulia Corporation.
- Alfano M, Furgiuele F, Leonardi A, Maletta C, Paulino G. 2009. Mode I fracture of adhesive joints using tailored cohesive zone models. *Int J Fract.* 157(1):193–204.
- Alterovitz R, Goldberg K, Okamura A. 2005. Planning for steerable bevel-tip needle insertion through 2D soft tissue with obstacles. In: *Robotics and Automation, 2005. ICRA 2005. Proceedings of the 2005 IEEE International Conference.* Barcelona, Spain. Piscataway (NJ): IEEE. p. 1640–1645.
- Azar T, Hayward V. 2008. Estimation of the fracture toughness of soft tissue from needle insertion. In: *Biomedical Simulation – 4th International Symposium, ISBMS 2008. Proceedings.* London, UK, July. Berlin/Heidelberg: Springer. p. 166–175.
- Chen J, Crisfield M, Kinloch AJ, Busso EP, Matthews FL, Qiu Y. 1999. Predicting progressive delamination of composite material specimens via interface elements. *Mech Comp Mater Struct.* 6(4):301–317.
- Chentanez N, Alterovitz R, Ritchie D, Cho L, Hauser KK, Goldberg K, Shewchuk JR, O'Brien JF. 2009. Interactive simulation of surgical needle insertion and steering. *ACM Transact Graph.* 28(3):1–10.
- Courtecuisse H, Jung H, Allard J, Duriez C, Lee DY, Cotin S. 2010. GPU-based real-time soft tissue deformation with cutting and haptic feedback. *Prog Biophys Mol Biol.* 103(2–3):159–168.
- DiMaio SP, Salcudean SE. 2002. Needle insertion modelling for the interactive simulation of percutaneous procedures. In: *Medical Image Computing and Computer-Assisted Intervention – MICCAI 2002. 5th International Conference. Proceedings, Part II.* Tokyo, Japan, September. Berlin (Germany): Springer-Verlag. p. 253–260.

- DiMaio SP, Salcudean S. 2003. Needle insertion modelling and simulation. *IEEE Transact Robot Automat.* 19(5):864–875.
- Franceschini G. 2006. The mechanics of human brain tissue [PhD Thesis]. Trento: University of Trento.
- Frasson L, Ko SY, Turner A, Parittotokkaporn T, Vincent JF, Rodriguez y Baena F. 2010. STING: a soft-tissue intervention and neurosurgical guide to access deep brain lesions through curved trajectories. *Proc IME H J Eng Med.* 224(6):775–788.
- Frick TB, Marucci DD, Cartmill JA, Martin CJ, Walsh WR. 2001. Resistance forces acting on suture needles. *J Biomech.* 34(10):1335–1340.
- Gao H, Klein P. 1998. Numerical simulation of crack growth in an isotropic solid with randomized internal cohesive bonds. *J Mech Phys Solids.* 46(2):187–218.
- Geißler G, Netzker C, Kaliske M. 2010. Discrete crack path prediction by an adaptive cohesive crack model. *Eng Fract Mech.* 77(18):3541–3557, DOI:10.1016/j.engfracmech.2010.04.029.
- Howard MA, Abkes BA, Ollendieck MC, Noh MD, Ritter C, Gillies GT. 1999. Measurement of the force required to move a neurosurgical probe through *in vivo* human brain tissue. *Biomed Eng IEEE Transact.* 46(7):891–894.
- Kataoka H, Washio T, Chinzei K, Mizuhara K, Simone C, Okamura AM. 2002. Measurement of the tip and friction force acting on a needle during penetration. In: *Medical Image Computing and Computer-Assisted Intervention – MICCAI 2002. 5th International Conference. Proceedings, Part I.* Tokyo, Japan, September. Berlin (Germany): Springer-Verlag. p. 216–223.
- Ko SY, Davies BL, Rodriguez y Baena F. 2010. Two-dimensional needle steering with a ‘Programmable Bevel’ inspired by nature: modelling preliminaries. In: *IEEE/RSJ International Conference on Intelligent Robots and Systems.* Taipei, Taiwan, October. Piscataway (NJ): IEEE. p. 2319–2324.
- Misra S, Reed KB, Douglas AS, Ramesh KT, Okamura AM. 2008. Needle-tissue interaction forces for bevel-tip steerable needles. In: *2nd IEEE RAS and EMBS International Conference on Biomedical Robotics and Biomechatronics, 2008. BioRob 2008.* Scottsdale, USA, October. Piscataway (NJ): IEEE. p. 224–231.
- Misra S, Reed KB, Schafer BW, Ramesh KT, Okamura AM. 2010. Mechanics of flexible needles robotically steered through soft tissue. *Int J Robot Res.* 29(13):1640–1660.
- Oldfield M, Dini D, Rodriguez y Baena F. 2010. Detailed finite element simulations of probe insertion into solid elastic material using a cohesive zone approach. In: *32nd Annual International Conference of the IEEE Engineering in Medicine and Biology Society (EMBC2010).* Buenos Aires, Argentina, September. Piscataway (NJ): IEEE. p. 3198–3201.
- Pannachet T, Sluys LJ, Askes H. 2009. Error estimation and adaptivity for discontinuous failure. *Int J Num Meth Eng.* 78(5):528–563.
- Sanford RJ. 2003. *Principles of fracture mechanics.* Upper Saddle River, NJ: Prentice Hall.
- Shergold O, Fleck NA. 2004. Mechanisms of deep penetration of soft solids, with application to the injection and wounding of skin. *Proceed Royal Soc Lon Series A Math Phys Eng Sci.* 460(2050):3037–3058.
- Shergold OA, Fleck NA. 2005. Experimental investigation into the deep penetration of soft solids by sharp and blunt punches, with application to the piercing of skin. *Transactions of the ASME. J Biomech Eng.* 127(5): 838–848.
- Simone C, Okamura AM. 2002. Modeling of needle insertion forces for robot-assisted percutaneous therapy. In: *Proceedings 2002 IEEE International Conference on Robotics and Automation.* Washington, DC, USA, May. Vol. 2. Piscataway (NJ): IEEE. p. 2085–2091.
- Song SH, Paulino GH, Buttlar WG. 2006. A bilinear cohesive zone model tailored for fracture of asphalt concrete considering viscoelastic bulk material. *Eng Fract Mech.* 73(18):2829–2848.
- Terada K, Ishii T, Kyoya T, Kishino Y. 2007. Finite cover method for progressive failure with cohesive zone fracture in heterogeneous solids and structures. *Comput Mech.* 39(2): 191–210.
- Vincent JFV, King MJ. 1995. The mechanism of drilling by wood wasp ovipositors. *Biomimetics.* 3(4):187–201.
- Wood NA, Shahrour K, Ost M, Riviere CN. 2010. Needle steering system using duty-cycled rotation for percutaneous kidney access. In: *32nd Annual International Conference of the IEEE Engineering in Medicine and Biology Society (EMBC2010).* Buenos Aires, Argentina, September. Piscataway (NJ): IEEE. p. 5432–5435.
- Zerbato D, Baschiroto D, Baschiroto D, Botturi D, Fiorini P. 2010. GPU-based physical cut in interactive haptic simulations. *Int J Comput Assist Radiol Surg.* 6(2): 265–272.
- Zhang Z, Ge X. 2005. A new quasi-continuum constitutive model for crack growth in an isotropic solid. *Europ J Mech A/Solids.* 24(2):243–252.